Phenomenological potentials for the refractory metals Cr, Mo and W

Gianguido Baldinozzi, Vassilis Pontikis

Phenomenological potentials for the refractory metals Cr, Mo and W

Gianguido Baldinozzi

Université Paris-Saclay, Centre National de la Recherche Scientifique, CentraleSupelec, Structures, Propriétés, et Modélisation des Solides, 91190 Gif-sur-Yvette, France

E-mail: gianguido.baldinozzi@centralesupelec.fr

Vassilis Pontikis

Université Paris-Saclay, Commissariat à l'Energie Atomique et aux Energies Alternatives, DRF/IRAMIS, 91191 Gif-sur-Yvette, France

E-mail: vassilis.pontikis@cea.fr

Abstract. Cohesion in the refractory metals Cr, Mo, and W is phenomenologically described in this work via a n-body energy functional with a set of physically motivated parameters that were optimized to reproduce selected experimental properties characteristic of perfect and defective crystals. The functional contains four terms accounting for the hard-core repulsion, the Thomas-Fermi kinetic energy repulsion and for contributions to the binding energy of s and d valence electrons. Lattice dynamics, molecular statics, and molecular dynamics calculations show that this model describes satisfactorily thermodynamic properties of the studied metals whereas, unlike other empirical approaches from the literature, predictions of phonon dispersion relations and of surface and point defect energetics reveal in fair good agreement with experiments. These results suggest that the present model is well adapted to large-scale simulations and whenever total energy calculations of thermodynamic properties are unfeasible.

PACS numbers: 63.20.D-, 61.72.J-, 65.40.De

Submitted to: *Journal of Physics: Condensed Matter*

1. Introduction

The refractory metals of the sixth column of the periodic classification of elements, Chromium (Cr), Molybdenum (Mo) and Tungsten (W) are of considerable practical interest for applications exploiting their outstanding properties including high melting temperatures, low thermal expansion, high thermal conductivity and mechanical resistance. Cr is used to harden steel, to manufacture stainless steel and as catalytic material [1], Mo is used in steel alloys to increase hardness, electrical conductivity and

resistance to corrosion and wear [2] whereas W is used in heating elements, in superalloys to form wear resistant coatings and in fusion reactors as plasma facing material capable to sustain the high heat loads [3, 4]. However, material properties evolve in time under working conditions emerging thereby the need for understanding and controlling ageing. To this end, a widely adopted approach consists in the atomistic modeling of ageing mechanisms via total energy calculations whenever the characteristic space scale of the phenomena of interest is small enough or via simulations relying on empirical potentials otherwise.

Phenomenological cohesion models are computationally performant in yielding well converged thermodynamical properties of large-sized systems from atomic scale simulations [5, 6, 7, 8], thus motivating the long-lasting efforts aimed at improving such models to faithfully reproduce physical properties of condensed matter [9, 6, 10, 11, 12, 13]. An extended and continuously growing literature attests for the increasing success of such approaches used in conjunction with open-source large-scale atomistic simulation packages that provide means for the seamless integration of existing and new empirical cohesion functionals [14].

The present work describes cohesion in Cr, Mo and W via semi-empirical analytic potentials with physically motivated repulsive and attractive terms. These apply to the refractory elements a recent approach (EGTB potentials), which has been shown outstandingly reproducing static, dynamic, and thermal properties of noble metals [13]. Unlike others [15, 16, 17, 18, 19], this model reproduces with remarkable accuracy the experimental phonon dispersion in these three metals. Moreover, the thermal expansion of the lattice and thermal atomic mean square displacements of the atoms (MSD) follow closely their experimental counterparts over an extended temperature range. These excellent characteristics suggest that the adopted potential form is well suited for large-scale simulations involving these three metals and that it is capable of faithfully reproducing the thermodynamic properties of these systems.

In difference with machine-learning approaches [20, 21], the methodology adopted here relies on a reduced set of adjustable and physically meaningful parameters spanning the cohesion energy of the studied system. The last is composed of four terms, namely: (i) a n-body attractive functional of the electron density deriving from the second moment approximation of the tight-binding scheme adapted to *d*-electron metals [9] (ii) a n-body attractive functional representing the *s*-electron contribution to cohesion (iii) a n-body repulsive functional akin to the kinetic energy term of the electron gas approximation [22, 13] and (iv) a short-range two-body repulsion that has been found crucially controlling the experimental equation of state, the surface energies, and the point defect energetics. The electron density entering the n-body functionals is described via atomic orbitals, this providing the recipe for generating potentials for any desired element. As is shown in the results section this methodology reproduces phonon dispersion with great accuracy and outstandingly well in the case of Mo and W, a result still out of reach of machine learning potentials [15].

The following paragraphs are devoted to the detailed description of the model

and its parametrization. The computational methods and techniques employed for the optimization of the parameters are also discussed. Calculated static, dynamic, and thermal properties of the three metals are presented and compared with experimental or with theoretical data, whenever experiments are not available. The final section details the strengths of the present approach and summarizes the main opportunities.

2. Model and computations

2.1. Model

In this cohesion model, the energy of atom i is the sum of four contributions involving the neighboring atoms j at distances $r_{ij} = \|\mathbf{r_j} - \mathbf{r_i}\|$:

$$U_i = U_{i,1}^{hc} + U_{i,2}^{TF} + U_{i,3}^{d} + U_{i,4}^{s} \tag{1}$$

The first term with superscript hc accounts for hard-core repulsive interactions. The second term with superscript TF represents the repulsive interactions of the electron kinetic energy. The two other terms represent attractive interactions related to s and d electrons respectively, both contributing to the cohesion energy of these transition metals [23, 22]. Hard-core interactions are empirically described by a cubic spline:

$$U_{i,1}^{hc} = \begin{cases} A_s \sum\limits_{j \neq i} \left[1 - \frac{r_{ij}}{r_s}\right]^3 & \text{if } r_{ij} \leq r_s \\ 0 & \text{otherwise} \end{cases} \tag{2}$$

This short-range term is crucially important because it controls the equation of state, the formation energies of interstitials, the thermal expansion, and to some extent the amplitudes of atomic MSD. Its form is purely empirical combining functional simplicity with the need of a rapidly vanishing with increasing the interatomic distance hard-core repulsion. It is a posteriori justified by the faithful reproduction of the aforementioned properties.

The second term was firstly introduced in a recent work dealing with the phenomenological modeling of cohesion in noble metals (EGTB potentials) [13]. This term aims at capturing the increase of repulsion between ions due to the increase of the kinetic energy of conduction electrons when the internuclear distances decrease [9]. This repulsive contribution is accounted for by a n-body functional mirroring the functional form for the kinetic energy of a non-interacting electron gas [22]:

$$U_{i,2}^{TF} = A_{TF} \left(\sum_{j \neq i} \rho_s \left(r_{ij} \right) \right)^{\frac{5}{3}} \tag{3}$$

where A_{TF} is an adjustable parameter and $\rho_s \left(r_{ij} \right)$ are the contributions of atoms j to the density of s-electrons at the location of atom i. This electron density is an explicit function of the positions of neighbors j that replaces the cruder uniform density approximation of the free-electron gas model.

The third term in Eq.(1) is a n-body non-additive term, formally similar to the expression of the density of d-electrons states obtained within the second moment approximation. This is the key ingredient for the description of the cohesion in transition metals (Friedel model [24, 23, 9]). Accordingly, this cohesive contribution to the energy of atom i is given by:

$$U_{i,3}^{d} = -\xi_d \left(\sum_{j \neq i} \rho_d \left(r_{ij} \right) \right)^{\frac{1}{2}} \tag{4}$$

where ξ_d is an adjustable parameter and $\rho_d \left(r_{ij} \right)$ are the contributions of atoms j to the d-electron density at the location of atom i. The related to this term interactions are empirically extended beyond the first neighbor distance, a precondition convincingly demonstrated by previous work [10, 13]. Although d-bonding dominates the cohesion energy of transition metals, valence s-electrons are also expected to contribute [25]. This contribution is expressed by the last term in Eq.(1) via a functional formally identical to $U_{i,3}^{d}$, with no other justification than computational convenience:

$$U_{i,4}^{s} = -\xi_s \left(\sum_{j \neq i} \rho_s \left(r_{ij} \right) \right)^{\frac{1}{2}} \tag{5}$$

where ξ_s is again treated as an adjustable parameter and $\rho_s \left(r_{ij} \right)$ is the density of s-electrons within the Voronoi cell of atom i. The reason for including this contribution in the cohesion energy stems from the empirical finding that it substantially improves the agreement between calculated and experimental phonon dispersion relations: in particular, the longitudinal and transversal [111] phonon-branches of Mo and W are drastically improved close to the symmetry point H of the Brillouin zone (Fig. 2). There is no justification of this choice but its operational capability in improving the computed phonon dispersion in Mo and W with respect to the experiments. This result is further discussed in section 3.2.

In most of the effective approaches of cohesion in transition metals, the electron density is usually represented via exponential or polynomial functions of the interatomic radial distances. Instead, the choice made in the present work consisted in using radial atomic orbitals adapted to each transition element. Thus, Cr(ρ_{3d}, ρ_{4s}), Mo(ρ_{4d}, ρ_{5s}) and W(ρ_{5d}, ρ_{6s}), functions were used with effective charges treated as adjustable parameters parameterizing these expressions (see Appendix). Since these atomic orbitals are long-range functions, quality that is not required for describing electron densities in metals, a multiplicative Fermi-Dirac screening is applied to the last for trimming these functions and thereby complying with the short-range behavior of the electron density in metals:

$$f_{FD}^{k}(r_{ij}) = \frac{1}{1 + \exp\left[\epsilon^{k} \left(\frac{r_{ij}}{r_0^{k}} \right) - 1 \right]} \tag{6}$$

where ϵ^{k} and r_0^{k} are adjustable parameters with values adapted to the corresponding s or d electron densities.

Table 1. Experimental data used in the potential parameterization: E_c and E_v are the energies of cohesion [27, 28] and of the vacancy formation [29, 30] respectively; a_0 is the lattice constant (expressed in nm) at zero pressure and at the temperatures T=0 K for Mo and W and T=77 K for Cr; B, C', and C_{44} are the bulk and shear elastic moduli (expressed in GPa). Lattice and elastic constants are taken from Ref. [31]. In italics between parentheses are reported the results from the best fit of the cohesion model against the experimental data. Formation energies of vacancies arise from unrelaxed states. The volume compression is $\delta = V/V_0$ where V_0, represents the volume at the atmospheric pressure and at temperature T=0 K.

Quantity	Cr	Mo	W
$E_c(eV/at)$	4.2(*4.18*)	6.81(*6.7*)	8.66(*8.64*)
$E_v(eV)$	2.0 − 2.4(*2.13*)	3±0.2(*3.27*)	4±0.3(*4.27*)
$a_0(nm)$	0.2881(*0.287*)	0.3143(*0.31405*)	0.3157(*0.3153*)
$B(GPa)$	190.1(*193.1*)	265.3(*234.3*)	314.15(*315.24*)
$C'(GPa)$	150.7(*147.0*)	138.5(*145.2*)	163.8(*164.76*)
$C_{44}(GPa)$	103.2(*95.2*)	125.0(*125.1*)	163.13(*163.9*)
Eq. of state [32]	δ / P(GPa)	δ / P(GPa)	δ / P(GPa)
	0.734/135.14	0.7936/95.24	0.685/260.66
	0.800/73.687	0.8106/83.257	0.755/160.59
	0.851/46.118	0.8550/56.378	0.801/111.24
	0.886/32.155	0.9178/27.005	0.855/68.280
	0.912/22.308	0.9568/12.584	0.898/42.500

2.2. Computational details

2.2.1. Geometric models and boundary conditions Crystal models employed in this work, for fitting the potential parameters or for running Molecular Dynamics (MD) simulations, were made of up to N≈15000 atoms. Thermal properties of systems such large have practically converged to their values at the thermodynamic limit, which has been shown by previous works for the formation energies of point defects and for the atomic MSD [26, 6]. The computational box edges have been chosen parallel to the cubic directions of the body centered cubic (bcc) lattice and periodic boundary conditions were applied along the three cartesian space directions X, Y, and Z. In calculations with free surfaces, the box size along the direction normal to the desired surface termination was fixed at a value on the least twice larger the corresponding thickness of the crystallite. Thereby, unphysical interactions between periodic images are avoided given the range of atomic interactions (see below Table 2).

2.2.2. Model parametrization The parameters of the model were determined using MERLIN, an open access multidimensional minimization package [33], driven by a user-defined routine that computes the cohesive energy, the hydrostatic pressure, and the elastic constants at the lattice constant value $a = a_0$ taken as the reference state with pressure value $p = 0$. Five other couples of pressure/volume values chosen from the

experimental equations of state[32] were used in the minimization scheme (Table 1). Given an initial set of model parameters, the driving routine computes the values of the cohesive energies at zero pressure of the body centered cubic (bcc), the face centered cubic (fcc), and the hexagonal compact (hcp) crystal structures; it also computes the unrelaxed formation energies of the vacancy, and of three configurations of split interstitials: $\langle 100 \rangle$, $\langle 110 \rangle$, and $\langle 111 \rangle$.

Initial trial values of the model parameters are adjusted via various algorithms that explore the directions in the vector space of parameters of the user-defined model; several algorithms are concurrently implemented in MERLIN and can be alternately employed for the numerical solution of these particular systems of equations. In the present case, the objective function is defined as the sum of squared differences between the calculated and the experimental values of the properties listed in Table 1. In this process, we required a supplementary condition on the cohesive energies ($E_c^{bcc} > E_c^{fcc}$ and $E_c^{bcc} > E_c^{hcp}$) to ensure the stability of the bcc structure over the competing fcc and hcp structures.

The lattice and elastic constants listed in this table are extrapolations of experimental data at finite temperatures: to $T = 0\ K$ for Mo and W, to $T = 77\ K$ for Cr [31]. The lattice constant values used for the model parametrization, displayed in italics, are linear extrapolations to $T = 0\ K$ of high-temperature data (T> θ_D, where, θ_D, is the Debye temperature). The minimization procedure converges when the differences between calculated and experimental properties is smaller then a chosen threshold value. The objective function yielding the potential parameters has in general several local minima. Not all of them are physically meaningful: the final assessment of the optimal parameter set is performed by comparing the model prediction to an extended set of experimental or theoretically inferred properties from the literature but also ensuring that the parameters of the model remain physically significant.

The final parameter sets for the three studied metals are summarized in Table 2. The bottom line displays the cutoff radii for the meaningful use in numerical simulations. It is worth remarking that the displayed values of ${r_c}^s$ and ${r_c}^d$ used in the radial density functions are effectively screened at distances shorter than the 4th neighbor distance. The flexibility of the cohesion model for fitting the properties of the studied metals is illustrated in Fig. 1 showing the good agreement between computed and experimental equations of state [32].

2.2.3. Molecular statics and dynamics MD calculations were performed in the isobaric-isothermal ensemble (NPT) with the combined Andersen [34] and Nosé [35] extended algorithms implemented in the MD home-made code operating via the central difference finite differences schemes of integration of the Newton equations of motion [36]. A time step $\delta t = 10^{-15} s$ warrants the conservation of the extended total Hamiltonian at better than 10^{-5}. The minimum linear dimensions of the computational boxes were always larger than twice the MD cutoff distances reported in Table 2. Thermal expansion and MSD as functions of the temperature were obtained via time averages over (NPT)-

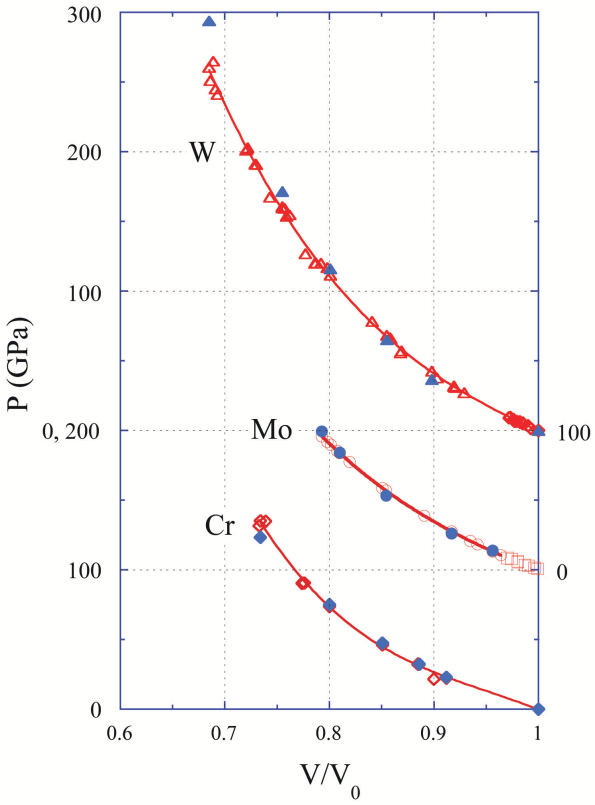

Figure 1. Equations of state: calculated (full diamonds, full circles, full triangles) and experimental [32] (open symbols). Full lines are cubic splines fitted on the experimental data serving as guides for the eye. Pressures scale in the intervals [0, 200] (Cr), [0, 300] (W)(left Y-axis), [0, 100] (Mo) (right Y-axis). The figure illustrates the flexibility of the model to satisfactorily adjust the equations of state of the three metals.

Table 2. Potential parameters: a_0 is the lattice constant at zero pressure and temperature. Cutoff radii for the hard-core repulsion (cubic spline), Fermi-Dirac screening (${r_c}^s$, ${r_c}^d$), and for molecular dynamics calculations (${r_c}^{MD}$) are expressed in a_0 units.

Quantity	Cr	Mo	W
a_0(nm)	0.287	0.31405	0.3153
A_{spline}(eV)	59.6	137.28	174.5
$r_{c-spline}$	0.88	0.868	0.872
A_{TF} (eV)	0.0	17.5	10423.61
Z_s	0.575	4.19	1.436
ξ_s(eV)	53.76	8.17	6.65
Z_d	0.79	2.93	2.946
ξ_d(eV)	18.94	27.62	53.23
ϵ_s	17.16	56.36	91.2
${r_c}^s$	1.05	1.492	0.99
ϵ_d	34.59	17.83	40.23
${r_c}^d$	1.066	1.0445	1.3

MD equilibrium trajectories that lasted 10^5 time steps. Energy minimizations at T=0 K, yielding relaxed surface and point defect formation energies, were performed with the same in-house MD package operating the quasi-dynamic minimization scheme with damping by setting to zero atom velocities if the value of the velocity-force scalar product is negative [37].

3. Results

3.1. Static properties

The formation energies of point defects and the values of the surface excess energy for three different surface terminations (100), (110), and (111) were obtained via energy minimization of the appropriate initial configurations (Table 3).

The predictions for the vacancy formation energies and surface energy are in reasonable good agreement with the experiments [29, 30, 38, 39, 40, 41, 42]. Given the formation energies of di-vacancies with the constitutive vacancies located at first nearest neighbor positions (1NN), the corresponding binding energy can be easily obtained and is also displayed in this table. It should be observed that E_b^{1NN} in W is quite close to the experimental result [43] whereas experimental values for Cr and Mo are not available. It is worth pointing out that some recent total energy calculations [15, 44, 45] report the binding energy of the di-vacancy in W at a value in disagreement with experiments. In particular, they predict the vacancy pair at 1NN position with almost vanishing binding energy and the value negative (repulsive) for the vacancy pair at 2NN position. Reasonable conclusions cannot be reached on this matter before the reason(s) why DFT calculations significantly diverge from the available experimental evidence are better understood [43].

The formation energies of interstitials for the studied metals and for various configurations are not available from experiments. They were presumed by using DFT results [51, 52]. These works question the former well-established belief that $\langle 110 \rangle$ split-interstitials represent the lowest energy configuration in most bcc metals, a view supported by a set of calculations relying on empirical many-body interatomic potentials. DFT calculations suggest the existence of systematic trends in the relative energies of formation of interstitials in various configurations in groups V and VI of bcc transition metals. In particular, in Mo and W the $\langle 111 \rangle$ configurations display the lowest energies whereas in Cr the $\langle 110 \rangle$ and $\langle 111 \rangle$ configurations have nearly the same energy of formation. The EGTB potentials developed in the present work reach a similar prediction for W, whereas they slightly favor the $\langle 110 \rangle$ configurations in Mo and Cr metals. The predicted absolute values of the formation energies are close to those provided by the DFT calculations (Table 3). However, it is worth emphasizing that none of these interstitials formation energies was entered as parameter in the model parameterization and that a re-parameterization including this piece of information could likely replicate the aforementioned trends. Nevertheless, this point is beyond

Table 3. Calculated values of: the stability of the bcc versus the *fcc* and *hcp* structures, point defect formation energies, E_v (vacancy), E_{2v}^{1NN} (di-vacancy), di-vacancy binding energies, split interstitials, E_{100}^{int}, E_{110}^{int} E_{111}^{int} and relaxed surface energies, E_s^{100}, E_s^{110}, E_s^{111}. ntal data are reported between parentheses in italics: Thermocalc lattice stability data from Refs. [46, 47, 48, 49], formation energies of vacancies and di-vacancies from Refs. [29, 30, 39, 38, 40, 41, 42] and the di-vacancy binding energy in W, $E_b^{1NN}(eV)$ from Ref. [43]. Experimental surface energies are recommended average values from Ref. [50]. Valuesbetween parentheses in bulk characters are estimations based on DFT calculations from Refs. [51, 52]

Quantity	Cr	Mo	W
$\delta E_{bcc/fcc}(eV)$	0.12(*0.108/0.278*)	0.27(*0.238/0.29*)	0.15(*0.109*)
$\delta E_{bcc/hcp}(eV)$	0.12	0.27(*0.02*)	0.15(*0.152*)
$E_{1v}(eV)$	2.04 (*2.0-2.4*)	2.82 (*2.24-3.0*)	4.18 (*3.14-4.0±0.3*)
$E_{2v}^{1NN}(eV)$			7.83 (**6.65**)
$E_b^{1NN}(eV)$			0.53 (*0.7*)
$E_{100}^{int}(eV)$	6.76 (**6.64**)	11.5 (**9.0**)	10.66 (**11.5**)
$E_{110}^{int}(eV)$	5.53 (**5.67**)	9.16 (**7.58**)	10.53 (**9.84**)
$E_{111}^{int}(eV)$	6.3 (**5.69**)	9.37 (**7.42**)	9.72 (**9.55**)
${E_s}^{100}(mJ/m^2)$	1864.3	2368.0	3216.2
${E_s}^{110}(mJ/m^2)$	1787.5	2323.4	2953.7
${E_s}^{111}(mJ/m^2)$	2252.4	2728.4	3755.1
${E_s}^{exp}(mJ/m^2)$	(*2090*)	(*2630*)	(*2690*)

the scope of the present work that only aims at testing the accuracy of the proposed cohesion model for describing bcc metals and comparing its strengths to other semi-empirical models.

Regarding surface energies, the present model exceeds the expectations of other models available in the literature that generally underestimate surface energies and fail to reproduce the correct order of stability of the low index surface terminations [53, 54]. Predicted energies of the low-index surface terminations are in fair good agreement with the experimental values [50]. However, the model favors the unreconstructed p(1x1) periodicity for all three low-index surfaces in contradiction with the experimental findings that clean Mo and W (100) facets are subjects to reconstruction [55, 56]. This failure marks one limit of the transferability of the present model and provides a possible direction for its further improvement.

3.2. Lattice dynamics

The accurate description of phonon dispersion relations has been a strong motivation of the present work that introduces a new class of empiric potentials for Cr, Mo, and W extending the library of potentials for these metals that already exist in the literature. Indeed, accurate phonon relations help in predicting reliable thermodynamic properties of crystals. Polymorphism and lattice instabilities are relevant problems in

many metallic systems [57]. The application of external pressure on such systems can drive these compounds towards or away from lattice instabilities, and several examples have been found relating tightly with peculiarities of dispersion plots often referred to as anomalies in the literature. Unlike other empirical potentials, the EGTB potentials meet this aforementioned objective. Figure 2 displays calculated harmonic phonon dispersion relations in the irreducible wedge of the Brillouin zone for these three transition metals at T=0 K. Experimental data points measured at room temperature taken from reference experiments are also shown [58, 59, 60]. The overall agreement is excellent excepted the [111] longitudinal branch in Cr predicted harder than is its experimental counterpart. Interestingly, the trends are satisfactory for the [111] transverse branches, except near the zone limits. It is worth mentioning the decisive role of the $U^s_{i,4}$ cohesive term in improving the agreement between computed and experimental branches in Mo and W. Indeed, without this cohesive term, a significant softening occurs of the force constants at the symmetry points H and N, the model failing to reproduce the experimental data.

The present cohesion model predicts a systematic reduction in the separation of the two non-degenerate transverse branches along the Σ line from Cr to Mo and W. The decreasing Zener anisotropy of the experimental elastic constants across the three metals is conceivably related to this behavior, which is captured by the present model including the degeneracy of the two transverse branches in the elastically isotropic W.

The present cohesion model outperforms other semi-empirical models: for instance, the bond-order potentials used to predict the dispersion relations of Mo and W by Čàk et al. [19] (dotted lines in Fig. 2) provide an example of the better behavior of EGTB potentials. Nevertheless, the systematic study of their exceeding performance against other potentials from the literature is beyond the scope of the present work. Moreover, there are still deviations between EGTB predictions and experimental data that underline the need for further refining the cohesion model. Two of such discrepancies are reported below and constitute a possible roadmap for further improvements:

(i) Along the $\Lambda([\xi\xi\xi])$ and $\Sigma([\xi\xi 0])$ longitudinal branches, especially at $k \geq 0.25$, the experimental frequencies in Mo and Cr are softer than predicted, an effect less pronounced in the case of W. On the basis of the band structure calculations by Asano et al. [61], Shaw et al. [59] attributed the strong depression of frequencies near the symmetry point N to the structure of the Fermi surface in Cr. More specifically, this anomaly proceeds from nesting portions of the Fermi surface, a feature suggested common to all the elements in this group [62, 63, 64].

(ii) The dispersion relations along the F line connecting the high symmetry points P and H, are correctly captured in Mo and W by the present cohesion model but not in Cr. In this metal, the transverse and longitudinal branches are almost degenerate, a feature that is not reproduced by the present model except near the point H where symmetry reasons impose branch degeneracy. Nevertheless, the EGTB potentials capture the correct shape of frequency eigenvalues along the Γ-H line.

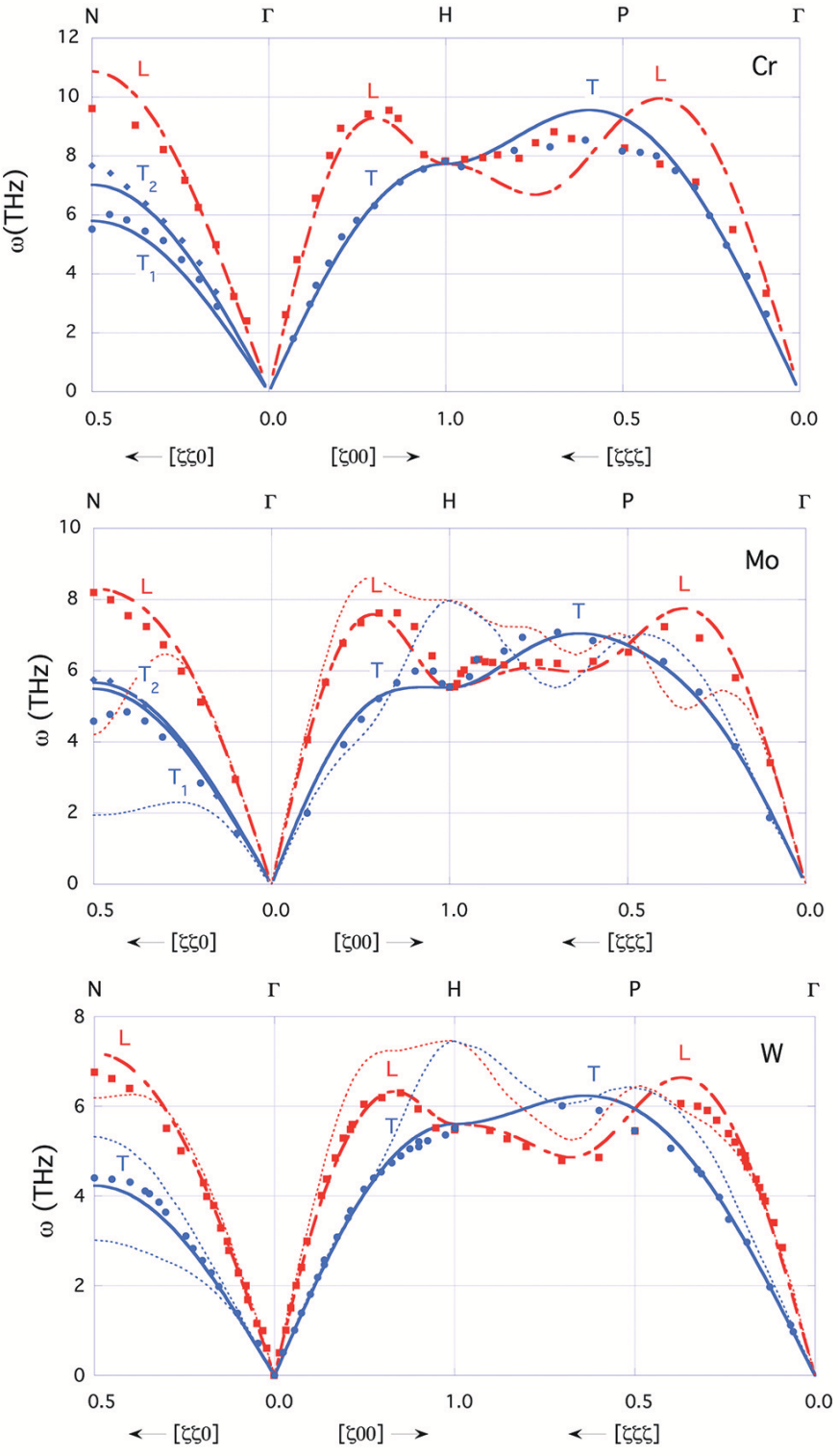

Figure 2. Comparison between experimental (full symbols) and calculated (full, dash-dotted and dotted lines) phonon dispersion curves. Experimental data are taken from: Refs.([59] (Cr), [60] (Mo), [58] (W)). The letters L (full squares, dash-dotted lines) and T (full circles, full lines) mark respectively longitudinal and transverse phonon modes. Full and dash-dotted lines: present work, dotted lines refer to the model of Ref. [19]. A very good agreement between the present calculations and the experiment is obtained, in particular for Mo and W metals.

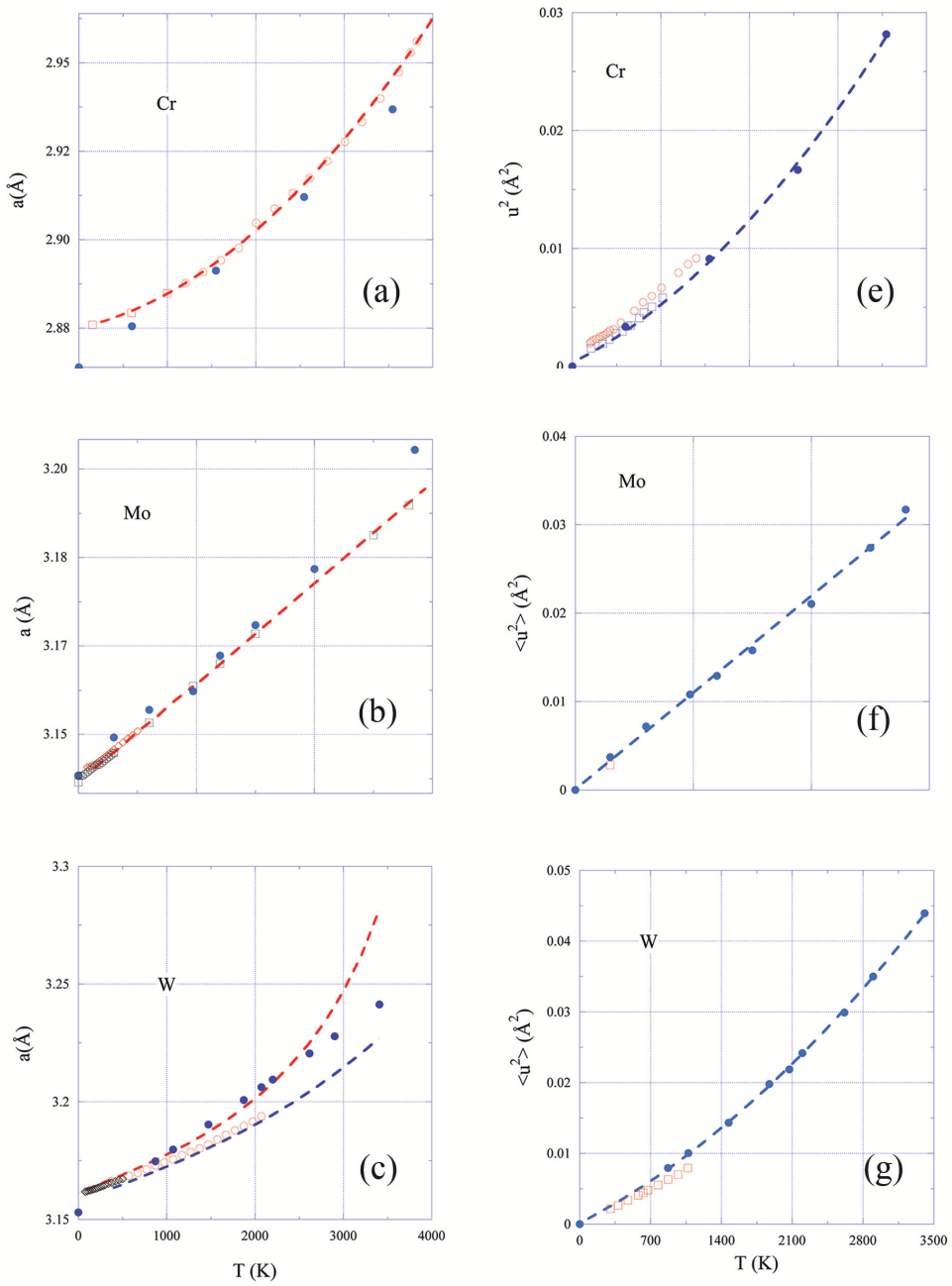

Figure 3. Comparison between experimental (open symbols) and calculated (full symbols) lattice constants (a-c) and atomic MSD (e-g) as functions of the temperature. Dashed lines are guides for the eye, left-hand side figures: linear or cubic spline fits on the experimental data, right-hand side figures: linear or parabolic fits on the MD data. Experimental lattice constants are taken from: Refs. [31, 65] (Cr), Ref. [31] (Mo), [31, 66] (W), and MSD from Refs. [67, 68] (Cr), [69] (Mo), and [70] (W).

3.3. Thermal properties

For the three studied metals, lattice constants a and atomic MSD's $< u^2 >= (u_x{}^2 + u_y{}^2 + u_z{}^2)/3$, were obtained as functions of the temperature from equilibrium trajectories in the (NPT) ensemble (Fig. 3, full symbols). For the comparison purpose, experimental values are also reported in this figure (open symbols).

Lattice constant predictions of the present model, as a function of the temperature, are in excellent agreement with the experimental data [31, 65, 66], except below the Debye temperature in Cr and W and at temperatures exceeding $\approx 0.7T_m$ in all the three metals, where T_m is the melting temperature. Similarly, atomic MSD calculated with the present model also reproduce satisfactorily the experimental data [70, 67, 69, 68], though this agreement should be considered with caution as experimental values are available only at modest temperatures (T<$0.3T_m$) and that only a single value has been reported in the literature for Mo [69]. It is worth emphasizing that a same level of accuracy was reached with the EGTB model of cohesion used for predicting in noble metals the lattice constant and MSD values as functions of the temperature [13], thus underlining the broader impact of the involved repulsion functionals and the prospective for a possible generalization to other elements.

4. Conclusive remarks

The model proposed in the present work differs from other existing phenomenological cohesion models because it introduces a repulsive functional of the many-body kinetic energy of electrons, a term better behaving than the widely used pairwise additive, inverse power or Born-Mayer exponential functions of the interatomic distance. It likely constitutes the reason of the performance of the EGTB models to match faithfully the surface energies and the trends observed when changing the surface crystallography. Similarly, lattice dynamics for these three bcc metals is reproduced with increased accuracy in comparison with experiments, thanks namely to the empirical finding that the s-electron contributions to cohesion control crucially phonon dispersion. Other phenomenological potentials are less successful in this respect. The fairly good agreement of calculated thermal properties with the experiment, ranks the potentials developed in this work among the best candidates for large-scale numerical simulations. The presence in these potentials of cubic spline terms allows for better describing short-range interactions that are important for reducing the gaps between calculated and experimental equations of state. These spline terms also improve the calculated formation energies of interstitials with respect to estimations based on total energy approaches. However, additional work is still required to better match the trends predicted by ab-initio calculations. We believe these further improvements will help to bridge the gap between simulations and experiments, making atomistic modeling more predictive and thereby getting closer to the long-term objective of developing materials-by-design via computations. The empirical potentials employed to describe

highly defective solids should capture not only pairwise contributions but also include the description of repulsive many-body effects. The many-body functional form of EGTB potentials is an essential ingredient of the successful modeling of defective solids as is illustrated by the very good predictions of surface and defect formation energies. In this context, simulations using EGTB potentials could be broadly employed to investigate mechanical properties of nano-structured materials and to detect nanoscale processes and structures, which are often inaccessible to experiments due to instrumental limitations of imaging techniques. Another related domain where EGTB-based simulation could bring promising results is the investigation of atomic-scale mechanisms controlling hardening and ductility of nano-structured metals. Finally, coupled with other multi-scale techniques, EGTB potentials could serve for studying the effect of loading rate on the mechanical response of metals and alloys.

5. Data availability statement

The data that support the findings of this study are available from the corresponding author upon reasonable request.

Acknowledgements

This work has been partially supported by a research grant of 'Investissements d'Avenir' of Labex PALM (ANR-10-LABX-0039-PALM). The authors are thankful to Ph. Chapelot, head of the Department of Nuclear Materials (DMN) of the Atomic Energy Commission (CEA) for the kind hospitality and his constant support.

Appendix A. Orbital equations

To cover every aspect describing the functions used in this paper, below are listed the expressions of the atomic wave functions (orbitals) entering the definition of the cohesive energy used in the present study of the transition refractory metals. These functions are extensively reviewed, commented and graphically illustrated in the literature and online [71]. In these functions the variable ρ is given by, $\rho = (2Zr/n)$ where, n is the principal quantum number, Z is the effective charge and, r is the distance expressed in atomic units (Bohr).

Appendix A.1. s-electron radial wave functions

$$R_{4s} = \frac{1}{96} \cdot \left(24 - 36\rho + 12\rho^2 - \rho^3\right) Z^{3/2} e^{-\rho/2} \tag{A.1}$$

$$R_{5s} = \frac{\sqrt{5}}{300} \cdot \left(120 - 240\rho + 120\rho^2 - 20\rho^3 + \right. \\ \left. + \ \rho^4\right) Z^{3/2} e^{-\rho/2} \tag{A.2}$$

$$R_{6s} = \frac{\sqrt{6}}{2160} \cdot \left(720 - 1800\rho + 1200\rho^2 - 300\rho^3 + \right.$$
$$\left. + \ 30\rho^4 - \rho^5\right) Z^{3/2} e^{-\rho/2} \tag{A.3}$$

Appendix A.2. d-electron radial wave functions

$$R_{3d} = \frac{\sqrt{30}}{9} \cdot \rho^2 Z^{3/2} e^{-\rho/2} \tag{A.4}$$

$$R_{4d} = \frac{\sqrt{5}}{96} \cdot (6 - \rho)\, \rho^2 Z^{3/2} e^{-\rho/2} \tag{A.5}$$

$$R_{5d} = \frac{\sqrt{70}}{150} \cdot \left(42 - 14\rho + \rho^2\right) Z^{3/2} e^{-\rho/2} \tag{A.6}$$

References

[1] J. Barnhart. Occurrences, uses and properties of chromium. *Regulatory Toxicology and Pharmacology*, 26:S3–S7, 1997. doi:10.1006/rtph.1997.1132.

[2] E. R. Braithwaite and J. Haber. *Molybdenum: An Outline of its Chemistry and Uses*. Elsevier Science B. V., Amsterdam, The Netherlands, 1994. (ISBN 0-444-88198-0).

[3] E. Lassner and W. D. Schubert. *Tungsten: Properties, Chemistry, Technology of the Element, Alloys, and Chemical Compounds*. Kluwer Academic/Plenum, New York, USA, 1999. (ISBN 0-306-45053-4).

[4] M. Rieth, S. L. Dudarev, and S. M. G. de Vicente at al. Recent progress in research on tungsten materials for nuclear applications in Europe. *J. Nucl. Mater.*, 432(3):482–500, 2013. doi:10.1016/j.jnucmat.2012.08.018.

[5] I. Yeh and G. Hummer. System-size dependence of diffusion coefficients and viscosities from molecular dynamics simulations with periodic boundary conditions. *J. Chem. Phys. B.*, 108:15873–15879, 2004. doi:10.1021/jp0477147.

[6] V. Rosato, M. Guillopé, and B. M. Legrand. Thermodynamical and structural properties of f.c.c. transition metals using a simple tight-binding model. *Philos. Pag. A.*, 59:321–336, 1989.

[7] R. Dovesi and R. Orlando. Convergence properties of the supercell approach in the study of local defects in solids. *Phase Transitions*, 52:151–167, 1994. doi:10.1080/01411599408201207.

[8] O. A. Moultos, Y. Zhang, I. N. Tsimpanogiannis, I. G. Economou, and E. J. Maginn. System-size corrections for self-diffusion coefficients calculated from molecular dynamics simulations. *J. Chem. Phys.*, 145:074109, 2016. doi:10.1063/1.4960776.

[9] F. Ducastelle. Modules élastiques des métaux de transition. *J. Physique*, 31:1055–1062, 1970. doi:10.1051/jphys:019700031011-120105500.

[10] F. Cléri and V. Rosato. Tight-binding potentials for transition metals and alloys. *Phys. Rev. B*, 48:22–33, 1993. doi:10.1103/PhysRevB.48.22.

[11] M. S. Daw and M. I. Baskes. Embedded-atom method: Derivation and application to impurities, surfaces, and other defects in metals. *Phys.Rev. B*, 29:6443–6453, 1984. doi:10.1103/PhysRevB.29.6443.

[12] M. I. Baskes. Determination of modified embedded atom method parameters for nickel. *Materials Chemistry and Physics*, 50:152–158, 1997. doi:10.1016/S0254-0584(97)80252-0.

[13] V. Pontikis, G. Baldinozzi, L. Luneville, and D. Simeone. Near transferable phenomenological n-body potentials for noble metals. *J Phys Condens Matter*, 29(35):355701, 2017. doi:10.1088/1361-648X/aa7766.

[14] S. Plimpton. Fast parallel algorithms for short-range molecular dynamics. *J. Comp. Phys.*, 117:1–19, 1995. doi:10.1006/jcph.1995.1039.

[15] J. Byggmastar, A. Hamedani, K. Nordlund, and F. Djurabekova. Machine-learning interatomic potential for radiation damage and defects in tungsten. *Phys.Rev. B*, 100:144105, 2019. doi:10.1103/PhysRevB.100.144105.

[16] K. Yang, L. Lang, H. Deng, F. Gao, and W. Hu. Modified analytic embedded atom method potential for chromium. *Modelling Simul. Mater. Sci. Eng.*, 26:065001, 2018. doi:10.1088/1361-651X/aaca48.

[17] C. Chen, Z. Deng, R. Tran, H. Tang, I. Chu, and S. P. Ong. Accurate force field by machine learning large materials data. *Phys. Rev. Materials*, 1:043603, 2017. doi:10.1103/PhysRevMaterials.1.043603.

[18] H. Park, M. R. Fellinger, T. J. Lenosky, W. W. Tipton, D. R. Trinkle, and S. P. Rudin. Ab-initio based empirical potential used to study the mechanical properties of molybdenum. *Phys. Rev. B*, 85:214121, 2012. doi:10.1103/PhysRevB.85.214121.

[19] M. Čàk, T. Hammerschmidt, J. Rogal, V. Vitek, and R. Drautz. Analytic bond-order potentials for the bcc refractory metals Nb, Ta, Mo and W. *J. Phys.: Condens. Matter.*, 26:195501, 2014.

[20] T. Mueller, A. Hernandez, and C. Wang. Machine learning for interatomic potential models. *J. Chem. Phys.*, 152:050902, 2020. doi:10.1063/1.5126336.

[21] A. Wood and A.P. Thompson. Extending the accuracy of the snap interatomic potential form. *J. Chem. Phys.*, 148:241721, 2018. doi:10.1063/1.5017641.

[22] Y. S. Kim and R. G. Gordon. Study of the electron gas approximation. *J. Chem. Phys.*, 60:1842–1850, 1974. doi:10.1063/1.1681283.

[23] J. Gyanchandani and S. K. Sikka. Physical properties of the 6d-series elements from density functional theory: Close similarity to lighter transition metals. *Phys. Rev. B.*, 83:172101, 2011. doi:10.1103/PhysRevB.83.172101.

[24] J. Friedel. Transitional metals. electronic structure of the d-band and its role in the crystalline and magnetic structure. In J. M. Ziman, editor, *The Physics of Metals: Volume 1, Electrons*, The Physics of Metals, pages 340–408, Cambridge, London and New York, 1969. Cambridge University Press. (ISBN 9780521071062).

[25] G. Frenking and N. Fröhlich. The nature of the bonding in transition-metal compounds. *J. Physique*, 100:717–774, 2000. doi:10.1021/cr9804011.

[26] F. Corsetti F and A. A. Mostofi. System-size convergence of point defect properties: The case of the silicon vacancy. *Phys. Rev. B*, 84:035209, 2011.

[27] Ch. Kittel. *Introduction à la Physique de l'Etat Solide*. Dunod, Paris, second edition, 1970. (Tableau I, p. 78).

[28] Jr. K. A. Gschneider. Physical properties and interrelationships of metallic and semi-metallic elements. *Sol. St. Phys.*, 16:275–426, 1964. (Table XII, p. 345).

[29] P. Ehrhart. 2.1.3.1 formation entropies and energies and equilibrium concentrations: Datasheet from landolt-börnstein - group iii condensed matter · volume 25: "atomic defects in metals" in springermaterials (https://doi.org/10.1007/10011948_31).

[30] K. Maier, M. Peo, B. Salle, H. F. Schaeffer, and A. Seeger. High–temperature positron annihilation and vacancy formation in refractory metals. *Philos. Mag. A*, 40:701–728, 1979.

[31] G. Simmons and H. Wang. *Single Crystal Elastic Constants and Calculated Aggregate Properties: A HANDBOOK*. The M.I.T. Press, Cambridge, Massachusetts and London, England, second edition, 1971.

[32] S. P. Marsh, editor. *LASL Shock Hugoniot Data*. University of California Press, Ltd., Berkeley - Los Angeles - London, 1991. (ISBN O-520-04008-2, Series ISBN: O-520-04007-4, Library of Congress Catalog Card Number: 79-65760).

[33] D. G. Papageorgiou, I. N. Demetropoulos, and I. E. Lagaris. Merlin-3.1.1. a new version of the merlin optimization environment. *Comput. Phys. Commun.*, 159:70–71, 2004. doi:10.1016/j.cpc.2003.12.005.

[34] H. C. Andersen. Molecular dynamics simulations at constant pressure and/or temperature. *J. Chem. Phys.*, 72:2384–2393, 1980. doi:10.1063/1.439486.

[35] S. Nosé. A molecular dynamics method for simulations in the canonical ensemble. *Mol. Phys.*, 52:255–268, 1984. doi:10.1080/00268978400101201.

[36] G. Ciccotti and J. P. Ryckaert. Molecular dynamics simulation of rigid molecules. *Comp. Phys. Rep.*, 4:345–394, 1986. doi:10.1016/0167-7977(86)90022-5.

[37] J. R. Beeler Jr. and G. L. Kulcinski. Agenda discussion: Computer techniques. In P. C. Gehlen, J. R. Beeler Jr., and R. I. Jaffee, editors, *Interatomic Potentials and Simulation of Lattice Defects*, pages 735–751, New York, 1972. Plenum. (ISBN 978-1-4684-1992-4).

[38] Ya. A. Kraftmakher. Vacancy formation energy in Mo. *Phys. Status Solidi*, 5:K48, 1964.

[39] Ya. A. Kraftmakher and P. G. Strelkov. Energy of formation and concentration of vacancies in W. *Soviet Phys. Solid State*, 4:1662–1664, 1963.

[40] F. Philipp, B. Saile, and K. Urban. Investigation of vacancy diffusion in niobium, molybdenum, and tantalum by means of high-voltage electron microscopy. In M. Doyama J.-I. Takamura and M. Kiritani, editors, *Point Defects and Defect Interactions in Metals*, pages 261–264, Tokyo, 1982. Tokyo University press.

[41] K.-D. Rasch, R. W. Siegel, and H. Schultz. Quenching and recovery experiments on tungsten. *J. Nucl. Mater.*, 69-70:622–624, 1978.

[42] M. Tietze, S. Takaki, J. A. Schwirtlich, and H. Schultz. Quenching investigations on b.c.c. transition metals. In M. Doyama J.-I. Takamura and M. Kiritani, editors, *Point Defects and Defect Interactions in Metals*, pages 265–267, Tokyo, 1982. Tokyo University press.

[43] J. Y. Park, H. C. W. Huang, R. W. Siegel, and R. W. Baluffi. A quantitative study of vacancy defects in quenched tungsten by combined field-ion microscopy and elecrtical resistometry. *Philos. Mag. A*, 48:397–419, 1983. doi:10.1080/01418618308234901.

[44] C. S. Becquart and C. Domain. Ab initio calculations about intrinsic point defects and He in W. *Nucl. Instrum. Methods Phys. Res. B*, 255:23–26, 2007. doi:10.1016/j.nimb.2006.11.006.

[45] K. Heinola1, 2 F. Djurabekova1, and T. Ahlgren. On the stability and mobility of di-vacancies in tungsten. *Nucl. Fusion*, 58:026004, 2018. doi:10.1088/1741-4326/aa99ee.

[46] Seh Kwang Lee and Dong Nyung Lee. Calculation of phase diagrams using partial phase diagram data. *Calphad*, 10:61–76, 1986. doi:10.1016/0364-5916(86)90010-6.

[47] R. Miedema and A. K. Niessen. The enthalpy of solution for solid binary alloys of two 4d-transition metals. *Calphad*, 7:27–36, 1983. doi:10.1016/0364-5916(83)90027-5.

[48] P. Nash. The cr-ni (chromium-nickel) system. *Bulletin of Alloy Phase Diagrams*, 7:466–476, 1986. doi:10.1007/BF02867812.

[49] N. Saunders, A. P. Miodownik, and A. T. Dinsdale. Metastable lattice stabilities for the elements. *Calphad*, 12:351–374, 1988. doi:10.1016/0364-5916(88)90038-7.

[50] V. K. Kumikov and Kh. B. Khokonov. On the measurement of surface free energy and surface tension of solid metals. *J. Appl. Phys.*, 54:1346–1350, 1983. doi:10.1063/1.332209.

[51] S. Han, L. A. Zepeda-Ruiz, G. J. Ackland, R. Car, and D. J. Srolovitz. Self-interstitials in V and Mo. *Phys. Rev. B*, 66:220101, 2002. doi:10.1103/PhysRevB.66.220101.

[52] A. P. Horsfield D. Nguyen-Manh and S. L. Dudarev. Self-interstitial atom defects in bcc transition metals: Group specific trends. *Phys. Rev. B*, 73:020101, 2006. doi:http10.1103/PhysRevB.73.020101.

[53] G. Bonny, D. Terentyev, A. Bakaev, P. Grigorev, and D. Van Neck. Many-body central force potentials for tungsten. *Model. Simul. Mater. Sci. Eng.*, 22:053001, 2014. doi:10.1088/0965-0393/22/5/053001.

[54] M. C. Marinika, L. Ventelon, M. R. Gilbert, L. Proville, S. L. Dudarev, J. Marian, G. Bencteux, and F. Willaime. Interatomic potentials for modelling radiation defects and dislocations in tungsten. *J. Phys. C: Condens. Matter*, 25:395502, 2013. doi:10.1088/0953-8984/25/39/395502.

[55] M. K. Debe and D. A. King. Space-group determination of the low-temperature w001(2x2)r45° surface structure by low-energy-electron diffraction. *Phys. Rev. Lett.*, 39(11):708–711, 1977. doi:10.1016/0039-6028(94)90692-0.

[56] P. J. Estrup. Surface phase of reconstructed tungsten (100) and molybdenum (100). *Surface Sci.*,

299-300:722–730, 1994. doi:10.1016/0039-6028(94)90692-0.

[57] M. T. Dove. *Introduction to Lattice Dynamics*. Cambridge Topics in Mineral Physics and Chemistry. Cambridge University Press, 1993. (doi: 10.1017/CBO9780511619885).

[58] A. Larose and B. N. Brockhouse. Lattice vibrations in tungsten at 22 °C studied by neutron scattering. *Can. J. Phys.*, 54:1819–1823, 1976. doi:10.1139/p76-215.

[59] W. M. Shaw and L. D. Muhlestein. Investigation of the phonon dispersion relations of chromium by inelastic neutron scattering. *Phys. Rev., B.*, 4:969–973, 1971.

[60] A. D. B. Woods and S.H. Chen. Lattice dynamics of molybdenum. *Solid State Comm.*, 2:233–237, 1964.

[61] S. Asano and J. Yamashita. Band theory of antiferromagnetic chromium. *J. Phys. Soc. Jpn*, 23:714–736, 1967. doi:10.1143/JPSJ.23.714.

[62] J. W. D. Connolly. The energy band structure of magnetic transition metals. *J. of Quantum Chem.*, 2S2:257–263, 1968. doi:10.1002/qua.560020725 .

[63] J. E. Graebner and J. A. Marcus. de haas-van alphen effect in antiferromagnetic chromium. *Phys. Rev.*, 175:659–673, 1968. (doi:10.1103/PhysRev.175.659).

[64] W M Lomer. Electronic structure of chromium group metals. *Proceedings of the Physical Society*, 80(2):489–496, aug 1962. doi:10.1088/0370-1328/80/2/316.

[65] Guy K. White and C. Andrikidis. Thermal expansion of chromium at high temperature. *Phys. Rev. B*, 53:8145–8147, 1996.

[66] G. K. White and M. L. Minges. Thermophysical properties of some key solids: An update. *Int. J. of Thermophysic*, 18:1269–1327, 1997.

[67] R. Kaplan and G. A. Somorjai. Observation of zero-point atomic motion near the cr (110) surface by low-temperature diffraction of slow electrons. *Solid State Comm.*, 9:505–509, 1970.

[68] R. H. Wilson, E. F. Skelton, and J. L. Katz. Measurementsof the thermal variation of the x-ray debye temperature of pure nickel and chromium. *Acta Cryst.*, 21:635–638, 1966.

[69] T. Paakkari. A determination of the debye-waller temperature factor and the x-ray debye temperature for Ni, Cr, Fe, Mo and W. *Acta Cryst. A*, 30:83–86, 1974.

[70] B.R.Bullard, J.G.Mullen, and G. Schupp. Mössbauer line-shape parameters for w and ir in metallic tungsten and iridium. *Phys.Rev. B*, 43(35):7405–7415, 1991. doi:10.1103/PhysRevB.43.7405.

[71] The orbitron, a gallery of orbitals. https://winter.group.shef.ac.uk/orbitron, 2021.